AIAA JOURNAL
Vol. 33, No. 7, July 1995

Comparison of Nonequilibrium Solution Algorithms Applied to Chemically Stiff Hypersonic Flows

Grant Palmer*
NASA Ames Research Center, Moffett Field, California 94035
and
Ethiraj Venkatapathy†
Eloret Institute, Palo Alto, California 94303

Three solution algorithms, explicit under-relaxation, point implicit, and lower-upper symmetric Gauss–Seidel, are used to compute nonequilibrium flow around the Apollo 4 return capsule at the 62-km altitude point in its descent trajectory. By varying the Mach number, the efficiency and robustness of the solution algorithms were tested for different levels of chemical stiffness. The performance of the solution algorithms degraded as the Mach number and stiffness of the flow increased. At Mach 15 and 30, the lower-upper symmetric Gauss–Seidel method produces an eight order of magnitude drop in the energy residual in one-third to one-half the Cray C-90 computer time as compared to the point implicit and explicit under-relaxation methods. The explicit under-relaxation algorithm experienced convergence difficulties at Mach 30 and above. At Mach 40 the performance of the lower-upper symmetric Gauss–Seidel algorithm deteriorates to the point that it is out performed by the point implicit method. The effects of the viscous terms are investigated. Grid dependency questions are explored.

Nomenclature

c	= speed of sound
c_s	= species mass fraction
c_∞	= freestream speed of sound
e	= total energy
h_s^o	= species heat of formation, J/kg
l_{ref}	= grid scaling reference length
M_s	= molar mass of species s, gm/mole
q_x, q_y, q_z	= heat conduction
R	= universal gas constant, 8.3144 J/mole-K
Re	= freestream Reynolds number, $\rho_\infty c_\infty l_{\text{ref}}/\mu_\infty$
t	= time, s
u, v, w	= Cartesian velocities
u_s, v_s, w_s	= Cartesian diffusion velocities
$\dot{w}_s$	= chemical source term
x, y, z	= Cartesian coordinates
κ	= thermal conductivity
μ	= viscosity
μ_∞	= freestream viscosity
ρ_s	= density of species s
ρ_∞	= freestream density
$\tau_{xx}, \tau_{xy}, \ldots, \tau_{zz}$	= shear stresses

Introduction

FUTURE human space exploration will require sending space vehicles to and from the moon, Mars, and beyond. The vehicles used to facilitate the return missions, whether aerobrakes or re-entry capsules, will be large diameter, blunt spacecraft that will re-enter the Earth's atmosphere at high velocity. Tauber et al.[1] performed trajectory studies on a 5-m-diam Mars return aerobrake that would enter the Earth's atmosphere at between 12 and 16 km/s and experience peak heating at between 64- and 68-km altitude. Lunar return vehicles will experience velocities in excess of 10 km/s. These spacecraft will often be traveling at an angle of attack creating a true three-dimensional flow environment.

Received Jan. 11, 1994; revision received Nov. 22, 1994; accepted for publication Dec. 10, 1994.

*Research Scientist, Aerothermodynamics Branch. Member AIAA.
†Research Scientist. Member AIAA.

Numerical algorithms will be used to calculate the aero- and thermal loads these vehicles will encounter. The combination of large body diameter and high-entry velocity creates near-equilibrium flow conditions in some regions of the computed shock layer. These conditions lead to numerical stiffness in the governing equations affecting the stability and robustness of the numerical algorithm used to calculate the flowfield. The computation of three-dimensional reacting flows is CPU intensive due to the complex physical models used and the large number of governing equations to be solved. The numerical algorithm must, therefore, also be efficient.

A considerable amount of research activity has been devoted to developing nonequilibrium flow codes that are both robust and efficient.[2–6] These codes have generally been tested and applied to flows above 70 km or to the reproduction of ground-based experiments.

This study tests the stability and convergence characteristics of three numerical algorithms when applied to very stiff flow conditions, a large diameter vehicle traveling at high velocity at an altitude of 62 km. The performance of each method is evaluated over a range of test conditions.

Governing Equations

The three-dimensional Navier–Stokes equations represent the conservation of mass, momentum, and energy. For chemical nonequilibrium flows, they include species continuity equations. The equations expressed in Cartesian coordinates are

$$\frac{\partial \hat{\boldsymbol{Q}}}{\partial t} + \frac{\partial \hat{\boldsymbol{E}}}{\partial x} + \frac{\partial \hat{\boldsymbol{F}}}{\partial y} + \frac{\partial \hat{\boldsymbol{G}}}{\partial z} = \frac{1}{Re}\left[\frac{\partial \hat{\boldsymbol{R}}}{\partial x} + \frac{\partial \hat{\boldsymbol{S}}}{\partial y} + \frac{\partial \hat{\boldsymbol{T}}}{\partial z}\right] + \hat{\boldsymbol{W}}$$

where

$$\hat{\boldsymbol{Q}} = \begin{bmatrix} \rho_1 \\ \vdots \\ \rho_n \\ \rho u \\ \rho v \\ \rho w \\ e \end{bmatrix} \qquad \hat{\boldsymbol{E}} = \begin{bmatrix} \rho_1(u+u_1) \\ \vdots \\ \rho_n(u+u_n) \\ \rho u^2 + p \\ \rho uv \\ \rho uw \\ (e+p)u \end{bmatrix}$$

Table 1 Specific heat curve fit constants

Species	a_1	a_2	a_3	a_4	a_5	a_6	a_7	a_8
N	2.4690	1.8827e-4	−1.7784e-7	5.9797e-11	−7.9413e-15	4.9765e-19	−1.4627e-23	1.6116e-28
O	2.7919	−3.1113e-4	1.1147e-7	−1.5967e-11	1.1444e-15	−4.1633e-20	6.4779e-25	0.0
NO	3.2943	1.1040e-3	−3.8424e-7	6.5532e-11	−5.5737e-15	2.4251e-19	−5.0930e-24	3.9301e-29
N_2	3.3141	1.0055e-3	−3.7609e-7	8.1710e-11	−1.0882e-14	8.7180e-19	−3.6331e-23	5.9153e-28
O_2	3.2489	1.372e-3	−5.2831e-7	1.1474e-10	−1.3237e-14	7.9561e-19	−2.3639e-23	2.7448e-28
NO^+	3.3277	9.2224e-4	−2.9325e-7	4.9489e-11	−5.0508e-15	3.6630e-19	−1.5729e-23	2.7385e-28
N_2^+	3.4070	4.503e-4	2.0053e-7	−8.8528e-11	1.370e-14	−1.0469e-18	3.9647e-23	−5.9278e-28
O_2^+	3.3036	1.0437e-3	−2.7916e-7	8.335e-12	7.1209e-15	−1.0151e-18	5.1945e-23	−9.2875e-28
O^+	2.5018	−1.2835e-5	2.279e-8	−1.3911e-11	3.5489e-15	−3.7052e-19	1.7067e-23	−2.8987e-28
N^+	2.6891	−3.0729e-4	1.5156e-7	−3.1635e-11	3.6498e-15	−2.3963e-19	8.3211e-24	−1.1783e-28
e^-	2.5	0.0	0.0	0.0	0.0	0.0	0.0	0.0

$$\hat{F} = \begin{bmatrix} \rho_1(v+v_1) \\ \vdots \\ \rho_n(v+v_n) \\ \rho uv \\ \rho v^2 + p \\ \rho vw \\ (e+p)v \end{bmatrix} \qquad \hat{G} = \begin{bmatrix} \rho_1(w+w_1) \\ \vdots \\ \rho_n(w+w_n) \\ \rho uw \\ \rho vw \\ \rho w^2 + p \\ (e+p)w \end{bmatrix}$$

$$\hat{R} = \left[0, \ldots, 0, \tau_{xx}, \tau_{xy}, \tau_{xz}, q_x + u_j\tau_{xj} - \sum_s \rho_s u_s h_s\right]^T$$

$$\hat{S} = \left[0, \ldots, 0, \tau_{xy}, \tau_{yy}, \tau_{yz}, q_y + u_j\tau_{yj} - \sum_s \rho_s v_s h_s\right]^T$$

$$\hat{T} = \left[0, \ldots, 0, \tau_{xz}, \tau_{yz}, \tau_{zz}, q_z + u_j\tau_{zj} - \sum_s \rho_s w_s h_s\right]^T$$

$$\hat{W} = [\dot{w}_1, \ldots, \dot{w}_n, 0, 0, 0, 0]$$

In the preceding expressions

$$u_j\tau_{xj} = u\tau_{xx} + v\tau_{xy} + w\tau_{xz}$$

Expressions for the shear stresses are provided in the Appendix.

The chemical source terms $\dot{w}_s$ represent the production of species from finite rate chemical reactions. In this study, a seven-species air chemistry model is used. This was chosen over an 11-species model in an effort to reduce computer time requirements. Charge neutrality is assumed throughout the flow, so only six species, (N, O, NO, N_2, O_2, NO^+), are included in the equation set. Six chemical reactions are evaluated to determine the species production terms. They are

$$N_2 + M \rightleftharpoons N + N + M$$

$$O_2 + M \rightleftharpoons O + O + M$$

$$NO + M \rightleftharpoons N + O + M$$

$$NO + O \rightleftharpoons N + O_2$$

$$N_2 + O \rightleftharpoons N + NO$$

$$N + O \rightleftharpoons NO^+ + e^-$$

The quantity M in the expressions can be any one of the species. Forward and backward reaction rates for the reaction set are obtained from Park.[7]

Pressure is obtained from the expression

$$p = \sum_s \frac{\rho_s}{M_s} RT \tag{1}$$

The equation relating temperature to total energy is

$$e = \sum_s \frac{\rho_s}{M_s} R \int c_{vs}\, dT + \sum_s \rho_s h_s^0 + \tfrac{1}{2}\rho(u^2 + v^2 + w^2) \tag{2}$$

Values of species specific heats c_{vs} are obtained by curve fit relations. Previously published specific heat curve fits[8,9] use a segmented approach; the curve fit is divided into temperature bands, each band employing a different mathematical relation to obtain the specific heat. Segmented curve fits can have discontinuities at the segment boundaries, and conditional relations must be incorporated into the code to identify which mathematical relation should be used.

An effort was undertaken to develop new curve fit relations that would provide accurate values of species specific heat with no segmentation of the curve fits. One mathematical expression is used throughout the entire temperature range, from 100 to 20,000 K. Under chemical nonequilibrium conditions, postshock temperatures will not exceed 20,000 K for any realistic Earth entry velocity. The curve relations take the form

$$C_p/R = a_1 + a_2T + a_3T^2 + a_4T^3 + a_5T^4 + a_6T^5 + a_7T^6 + a_8T^7 \tag{3}$$

The constants were obtained by matching reference values for C_p/R at eight temperatures from 0 to 20,000 K. Below 6000 K the reference values were taken from JANAF thermochemical data.[10] Reference values for the neutral diatomic species, N_2, O_2, and NO, above 6000 K were calculated by Jaffe,[11] using rigorous quantum mechanical definitions of the molecular partition functions. Reference values for the atomic and ionized diatomic species above 6000 K were taken from Ref. 8.

Because no segmentation is used, the specific heat curve is continuous throughout the entire temperature range. Species enthalpy or internal energy can be obtained by integrating Eq. (3). Values of the constants, $a_1, a_2, \ldots, a_8$, for 11-species air are listed in Table 1.

Nondimensional Numbers

Two nondimensional parameters are used in the analyses presented in this paper. The first is the Damkohler number defined as

$$D_a = \tau_{\text{trans}}/\tau_{\text{chem}} \tag{4}$$

The quantity τ_{trans} is the characteristic time of translation. It can be evaluated for each computational cell by dividing the length of the cell by the mean flow velocity. The parameter τ_{chem} is the characteristic time of chemical relaxation. This can be computed for each chemical reaction and is a function of total density, species density, and temperature. Two limiting cases of Damkohler number are if $D_a \ll 1$, the flow can be considered frozen, and if $D_a \gg 1$, the flow is in chemical equilibrium.

The second nondimensional number used in this study is the Courant–Friedrichs–Lewy (CFL) number defined as

$$\text{CFL} = |\lambda_{\max}|\Delta t/\Delta x$$

where $\lambda_{\max}$ is the maximum of the eigenvalues. Explicit methods cannot run at a time step that yields a CFL number greater than one. Implicit methods can run at CFL numbers greater than one.

Solution Algorithms

The governing equations are transformed from Cartesian (x, y, z) to a generalized (ξ, η, ζ) coordinate system. The generalized Navier–Stokes equations are

$$\frac{\partial \boldsymbol{Q}}{\partial t} + \frac{\partial \boldsymbol{E}}{\partial \xi} + \frac{\partial \boldsymbol{F}}{\partial \eta} + \frac{\partial \boldsymbol{G}}{\partial \zeta} = \frac{1}{Re}\left[\frac{\partial \boldsymbol{R}}{\partial \xi} + \frac{\partial \boldsymbol{S}}{\partial \eta} + \frac{\partial \boldsymbol{T}}{\partial \zeta}\right] + \boldsymbol{W}$$

The transformed $\boldsymbol{Q}$ and $\boldsymbol{W}$ vectors are given by

$$\boldsymbol{Q} = \hat{Q}/J \qquad \boldsymbol{W} = \hat{W}/J$$

and the transformed flux vectors are

$$\boldsymbol{E} = \frac{\xi_x \hat{E} + \xi_y \hat{F} + \xi_z \hat{G}}{J} \qquad \boldsymbol{R} = \frac{\xi_x \hat{R} + \xi_y \hat{S} + \xi_z \hat{T}}{J}$$

$$\boldsymbol{F} = \frac{\eta_x \hat{E} + \eta_y \hat{F} + \eta_z \hat{G}}{J} \qquad \boldsymbol{S} = \frac{\eta_x \hat{R} + \eta_y \hat{S} + \eta_z \hat{T}}{J}$$

$$\boldsymbol{G} = \frac{\zeta_x \hat{E} + \zeta_y \hat{F} + \zeta_z \hat{G}}{J} \qquad \boldsymbol{T} = \frac{\zeta_x \hat{R} + \zeta_y \hat{S} + \zeta_z \hat{T}}{J}$$

The quantity J in the expressions is the Jacobian of the coordinate transformation.

The simplest solution algorithm is the explicit Euler algorithm. This method evaluates the flux and source term vectors at the current, or n, time step. The three-dimensional explicit Euler solution algorithm written in generalized coordinates is

$$\delta \boldsymbol{Q} = -\Delta t[\delta_\xi \boldsymbol{E} + \delta_\eta \boldsymbol{F} + \delta_\zeta \boldsymbol{G} - \boldsymbol{W} - (1/Re)(\delta_\xi \boldsymbol{R} + \delta_\eta \boldsymbol{S} + \delta_\zeta \boldsymbol{T})] \quad (5)$$

where

$$\delta \boldsymbol{Q} = \boldsymbol{Q}^{n+1} - \boldsymbol{Q}^n$$

The term δ_ξ indicates a spatial difference in the ξ direction. If no source term is present, this method has a maximum allowable CFL number, based on the fluid dynamics, of one.

For nonequilibrium flows, the species production terms obtained from finite rate chemical reactions introduce an additional stiffness into the equation set causing the algorithm to be unstable except for very small CFL numbers. For this reason, the explicit Euler solution algorithm is widely regarded as unsuitable for the computation of nonequilibrium flows.

To overcome the time step restrictions imposed by the chemical source terms, the source terms can be evaluated implicitly, at the $n+1$ time step. A Taylor series expansion is performed on this term and the resulting algorithm, called point or chemistry implicit, is given by

$$\left[I - \Delta t \frac{\partial \boldsymbol{W}}{\partial \boldsymbol{Q}}\right]\delta \boldsymbol{Q} = \text{RHS} \quad (6)$$

where the right-hand side (RHS) in Eq. (6) contains the explicit terms, the elements on the right-hand side of Eq. (5). In this study the inviscid flux differences are evaluated using Van Leer flux vector splitting.[12] Full viscous terms are included as well as a binary diffusion model.

This algorithm is called the point implicit method because the implicit terms are not spatially differenced but are evaluated point by point. Because the chemistry terms are handled implicitly, this algorithm has a CFL number limitation of one.

To achieve CFL numbers greater than one, it is necessary to evaluate the fluid dynamic flux terms implicitly. One method that has gained popularity in recent years is the lower-upper symmetric Gauss–Seidel (LUSGS). It was developed by Yoon and Jameson.[13] The method splits the Jacobian matrices, $A = (\partial \boldsymbol{E}/\partial \boldsymbol{Q})$, $B = (\partial \boldsymbol{F}/\partial \boldsymbol{Q})$, and $C = (\partial \boldsymbol{G}/\partial \boldsymbol{Q})$, into positive and negative components and factors the resulting split matrices into three submatrices. The resulting algorithm is given by

$$LDU\delta \boldsymbol{Q} = \text{RHS} \quad (7)$$

where

$$L = I + \Delta t\left[[r_a + r_b + r_c]I - A^+_{i-1} - B^+_{j-1} - C^+_{k-1} - \frac{\partial \boldsymbol{W}}{\partial \boldsymbol{Q}}\right]$$

$$D = [I + \Delta t([r_a + r_b + r_c]I)]^{-1}$$

$$U = I + \Delta t[[r_a + r_b + r_c]I + A^-_{i+1} + B^-_{j+1} + C^-_{k+1}]$$

The approximate split flux Jacobians A^+ and A^- are computed from the equation

$$A^\pm = (A \pm r_a I)/2 \quad (8)$$

where r_a is the spectral radius equal to the absolute value of the largest eigenvalue,

$$r_a = |U| + c\sqrt{\xi_x^2 + \xi_y^2 + \xi_z^2} \quad (9)$$

In Eq. (10), U is the contravariant velocity in the ξ direction, $\xi_x u + \xi_y v + \xi_z w$. Similar expressions are used to calculate the $B\pm$ and $C\pm$ matrices. To obtain $\delta \boldsymbol{Q}$, the $[L]$ and $[U]$ elements are solved by sweeping from one corner of the computational domain to the other. One matrix inversion is required per point per step because the $(\partial \boldsymbol{W}/\partial \boldsymbol{Q})$ matrix must be inverted.

The third method tested was developed by Palmer.[14] This technique maintains the stability of a nonequilibrium algorithm within the context of the explicit formulation. This explicit under-relaxation algorithm evaluates the species density equations as well as the total density conservation equation explicitly. From these equations the changes in species mass fractions are calculated

$$\delta c_i = (\delta \rho_i - c_i \delta \rho)/\rho \quad (10)$$

If the absolute value of the maximum change in species mass fraction is greater than a prescribed value *tol* then the changes in species mass fraction are scaled

$$\delta c_i = \frac{\delta c_i}{|\delta c_{\max}|} * tol \quad (11)$$

The parameter *tol* is an under-relaxation factor with a value between 0 and 1. Additionally, no species mass fraction is allowed to become negative. Species densities are updated by

$$\rho_i^{n+1} = c_i^{n+1} \rho^{n+1} \quad (12)$$

In effect, this technique reduces the chemistry time step in regions of stiffness and has been applied to a variety of hypersonic flow computations.[6,14,15]

Boundary Conditions

The boundary conditions used in the calculations to come were as follows: Along the inflow ($k = k$ max) plane, freestream values are maintained. Symmetry conditions are used for the $j = 1$ and $j = j$ max planes. Along the outflow ($i = i$ max) plane and along the singular line ($i = 1$), values are obtained by extrapolation. A constant temperature of 1500 K was maintained on the body surface that was assumed to be noncatalytic. Nonslip and zero pressure gradient conditions were enforced.

Implicit boundary conditions are incorporated into the LUSGS option. At the body surface, they are based on the relations

$$\delta p_1 = \delta p_2 \qquad \delta T_1 = 0 \qquad \delta c_{s1} = \delta c_{s2}$$

$$\delta \rho u_1 = \delta \rho v_1 = \delta \rho w_1 = 0$$

The subscript 1 in the preceding relations refers to the body surface and the 2 to the next interior plane. The expressions are used to obtain values of $\delta \boldsymbol{Q}$ at the body surface.

Results

Specific Heat Data

Results generated using the new curve fit relations are compared against two previously published segmented curve fits. Balakrishnan[8] developed curve fit relations up to 50,000 K using from five to seven temperature bands. The curve fits have the form

$$C_p = a + bT + c/T^2 \tag{13}$$

The second curve fit relations, used by Gnoffo et al.,[9] have the form

$$C_p/R = a_1 + a_2T + a_3T^2 + a_4T^3 + a_5T^4 \tag{14}$$

and are used to calculate species specific heats up to 35,000 K using five temperature bands.

Figure 1a compares values of the specific heat of atomic nitrogen calculated using the three curve fit relations. The segmented curve fits exhibit discontinuities at the temperature band interfaces, particularly at 6,000 and 10,000 K. The nonsegmented curve fit is continuous throughout the entire temperature range and reproduces the JANAF specific heat data with a maximum error of 2.2%. At temperatures above 6,000 K, the three curve fits give similar data, except for the Balakrishnan curve fit in the temperature range of 10,000–15,000 K.

Figure 1b shows specific heat data for NO. Again the segmented curve fits show discontinuities at the 3,000, 6,000, and 10,000 K temperature band segment interfaces. Above 12,000 K only the unsegmented curve fit relations match the reference values of Jaffe,[11] which include effects such as a nonrigid rotor rotational model and vibration–rotation coupling. Vibration–rotation coupling produces a significant negative contribution to the specific heat of nitric oxide above 12,000 K. The nonsegmented curve fit values are in good agreement with the reference values along the entire temperature range.

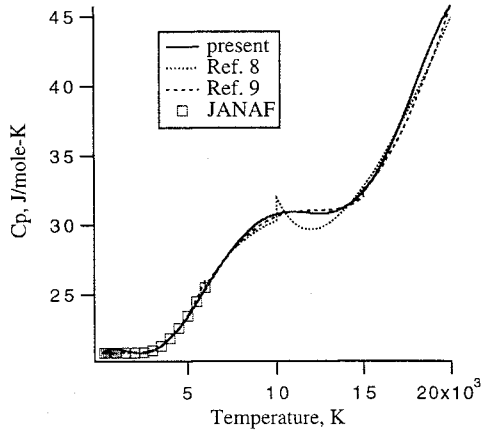

a)

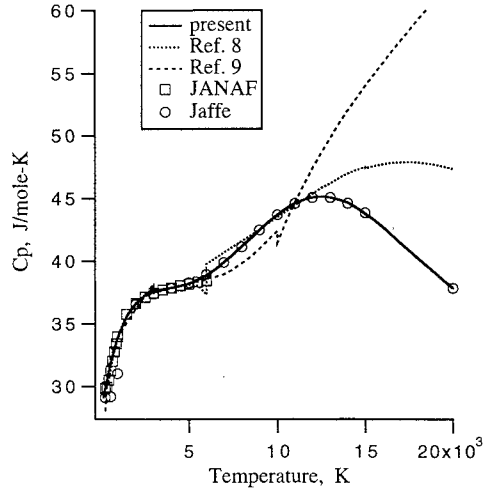

b)

Fig. 1 Specific heat comparison: a) atomic nitrogen and b) nitric oxide.

Solution Algorithm Comparisons

The solution algorithms were tested by computing flow over the base of the Apollo 4 return capsule at the 62-km-altitude point along its descent trajectory. The capsule geometry is the intersection of a 4.69-m-radius sphere with a 33-deg half-angle cone.[16] The cone–sphere intersection is rounded into a 19.56-cm-radius shoulder. The freestream conditions at 62 km are given as

$$r_n = 4.69\,\text{m}$$

$$\rho_\infty = 2.407 \times 10^{-4}\,\text{kg/m}^3$$

$$p_\infty = 16.69\,\frac{\text{nt}}{\text{m}^2}$$

$$T_\infty = 241.5\,\text{K}$$

$$c_\infty = 311.5\,\text{m/s}$$

$$\text{mass fraction } N_2 = 0.7656$$

$$\text{mass fraction } O_2 = 0.2344$$

By varying the freestream Mach number, it is possible to simulate different levels of chemical stiffness. Table 2 displays the computed postshock stagnation line Damkohler number at 62 km for each of the six chemical reactions at Mach numbers of 15, 30, and 40. Mach 40 corresponds to a freestream velocity of 12.5 km/s. For most of the reactions, the Damkohler number increases with increasing Mach number. Increasing Damkohler number indicates increasing chemical stiffness. The ionization of nitric oxide reaction is the stiffest reaction at Mach 30. The Damkohler number of the thermal dissociation of nitric oxide reaction, reaction 3, increases more than an order of magnitude with each increased Mach number and is the stiffest reaction at Mach 40. There is a large increase in Damkohler number for reactions 1, 2, 3, and 6 when the Mach number is increased from 30 to 40. This is in part due to the fact that the seven-species model is inadequate at 12.5 km/s and leads to unrealistically high postshock temperatures.

The 49 × 11 × 49 grid used in the first set of parametric studies is shown in Fig. 2. Only every third grid line in the body normal and streamwise directions are shown for figure clarity. Calculations

Table 2 Postshock stagnation line Damkohler number, 62 km

	Mach = 15	Mach = 30	Mach = 40
$N_2+M=N+N+M$	6.8×10^{-4}	0.38	97.9
$O_2+M=O+O+M$	5.1	67.2	363
$NO+M=N+O+M$	0.82	246	10,180
$NO+O=N+O_2$	4.1	103	44.7
$N_2+O=N+NO$	43.7	67	18.4
$N+O=NO^+ + e^-$	91.1	463	989

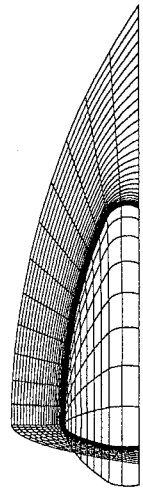

Fig. 2 49 × 11 × 49 grid.

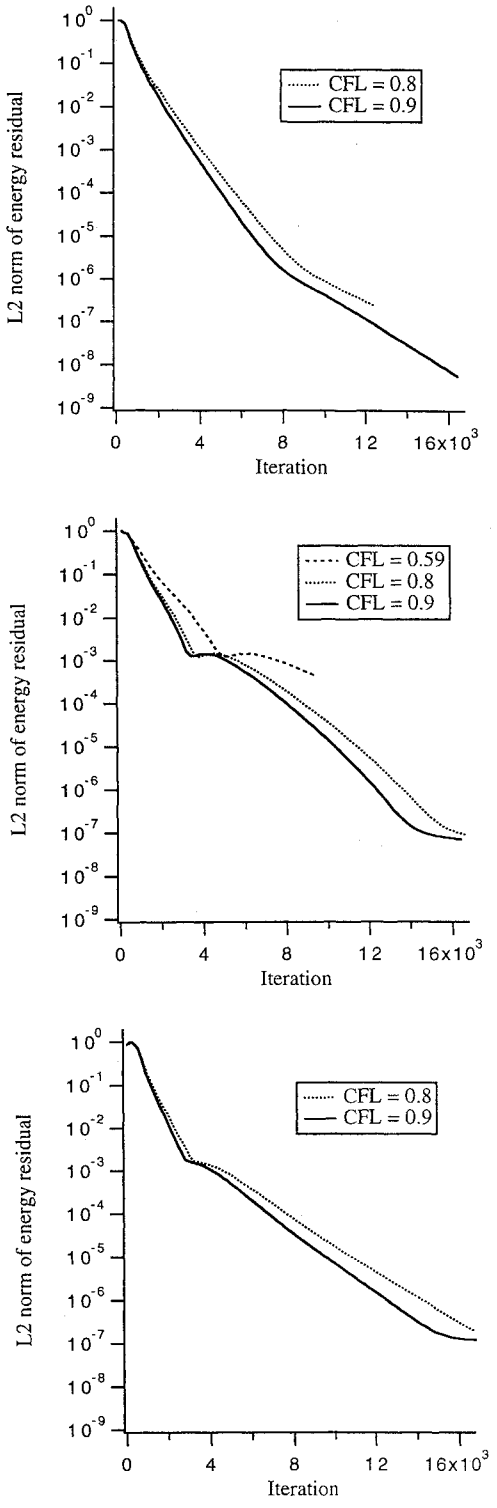

Fig. 3 Convergence histories, point implicit method: a) Mach 15, b) Mach 30, and c) Mach 40.

performed using this grid were performed at zero angle of attack so only a 90-deg section of the Apollo vehicle is used.

Figure 3 presents convergence histories of the point implicit method at Mach 15, 30, and 40. In these and subsequent figures, the maximum level of residual for each calculation was scaled to unity to aid the comparison at different Mach numbers. Figure 3a shows the results at Mach 15. The point implicit solution converges in a smooth manner while running at maximum CFL numbers of 0.8 and 0.9. The $L2$ norm of the energy residual, defined as the square root of the sum of the energy residual at each point in the computational domain squared, converges eight orders of magnitude after running 16,000 steps at CFL = 0.9.

At Mach 30, the stiffness of the chemistry terms increases. As shown in Fig. 3b, the convergence rate at a CFL number of 0.9 slows after a three order of magnitude drop in residual. The rate of convergence then increases but slows again after converging an additional four orders of magnitude. Lowering the CFL number did not eliminate the decrease in the rate of convergence. This same behavior is apparent when the maximum CFL number was reduced to 0.8 and 0.59. The overall convergence rate of the point implicit method is slightly less than that seen at Mach 15.

Results when the point implicit method was run at Mach 40 are shown in Fig. 3c. The performance of the method is similar to that seen at Mach number 30 except the second decrease in the rate of convergence occurs at a later point in the computation.

The performance of the explicit under-relaxation method is examined in Fig. 4. The value of the under-relaxation parameter *tol* seen in Eq. (11) was set to 0.01. The convergence histories for Mach 15 are shown in Fig. 4a. The solution converges in a smooth manner at maximum CFL numbers of 0.55, 0.68, and 0.8, but when the CFL number is raised to 0.9 the convergence profile flattens out after dropping just over three orders of magnitude.

When the Mach number is raised to 30 the convergence difficulties occur even when the CFL number is reduced to 0.27. This is shown in Fig. 4b. The oscillating behavior of the residual is clearly evident at CFL numbers of 0.6 and 0.8. The same trend was seen at Mach 40. For no value of CFL number would the solution converge.

The explicit under-relaxation algorithm is an approximate method. The under-relaxation parameter *tol* has the same effect as the implicit chemistry matrix does in the point implicit algorithm. Evaluating the species density updates using *tol* is not as rigorous or as time consuming as filling and inverting the implicit chemistry matrix. When the chemistry is not very stiff this approximate nature does not adversely affect the solution process. When the chemistry becomes stiff the explicit under-relaxation method breaks down. What happens is that the code over- or undershoots the proper chemical state of the gas, and the solution oscillates between two chemical states. This happens throughout the flowfield but particularly in regions of high chemical stiffness. The explicit under-relaxation method never converges to a single steady-state solution.

A parametric study on the under-relaxation parameter *tol* was performed at Mach 30 to see if the value of the parameter affected the convergence rate of the method. Figure 4c shows the convergence histories obtained using three values of the under-relaxation parameter. All three residuals flatten out and begin an oscillatory behavior. The solution using the lowest value of *tol*, 0.001, converges nearly one order of magnitude further before flattening out, but none of the *tol* values permitted full convergence to occur.

Comparing Figs. 3 and 4, both the point implicit and the explicit under-relaxation methods experience a leveling off of the rate of convergence at Mach 30. The point implicit is able to overcome this after some time and then is able to continue to converge. The explicit under-relaxation cannot, and the solution from this point oscillates.

The performance of the LUSGS algorithm is presented in Fig. 5. Figure 5a shows the convergence histories at Mach 15. At maximum CFL numbers of 20, 40, and 90, smooth convergence is achieved. The method became unstable, however, when the CFL number was increased to 180.

Figure 5b shows the convergence histories at Mach 30. The residual curve now flattens after converging three orders of magnitude. The residual then drops another three orders of magnitude at this reduced rate before dropping rapidly for about 300 iterations after which the residual curve flattens out again. The performance of the LUSGS method diminished when the Mach number was increased from 15 to 30. At Mach 30, 50% more iterations were required to achieve the level of convergence obtained at Mach 15. Lowering the CFL number did not affect the shape of the residual profile.

The performance of the LUSGS method degrades severely at Mach 40, shown in Fig. 5c. When the algorithm was run at a CFL number of 23, the residual profile leveled off after converging two orders of magnitude, similar to the behavior seen with the explicit under-relaxation method. The convergence problem remained when the CFL number was reduced to 5.8. Only when the CFL number was reduced to 2.3 did the performance improve. At a CFL number

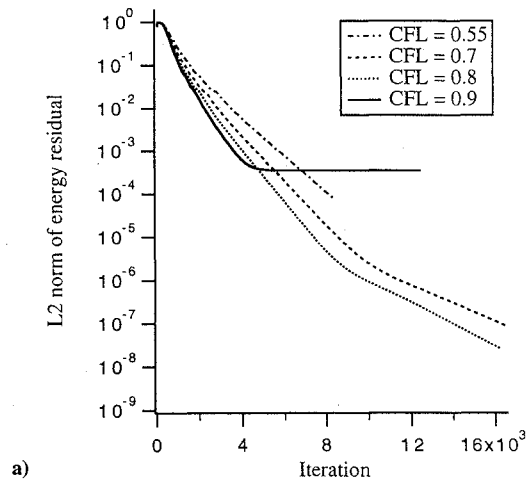

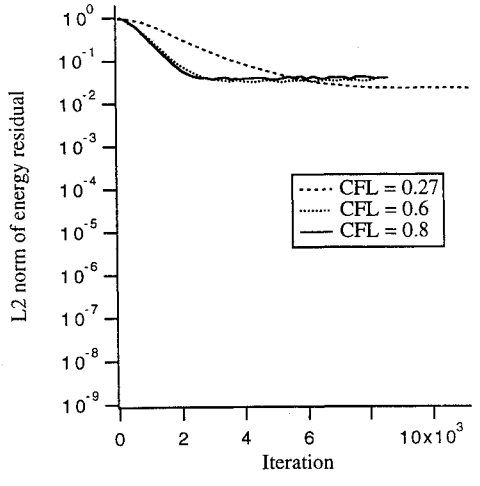

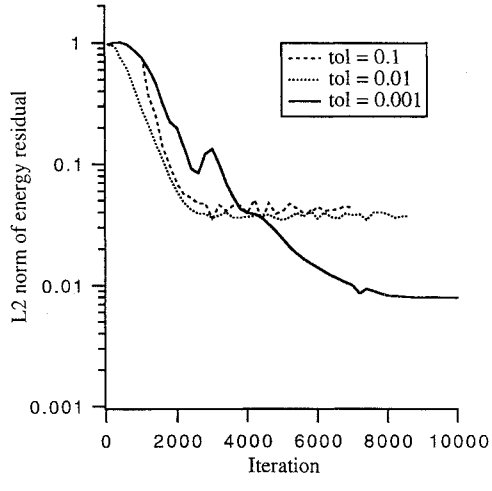

Fig. 4 Convergence histories, explicit under-relaxation method: a) Mach 15, b) Mach 30, and c) constant parametric study.

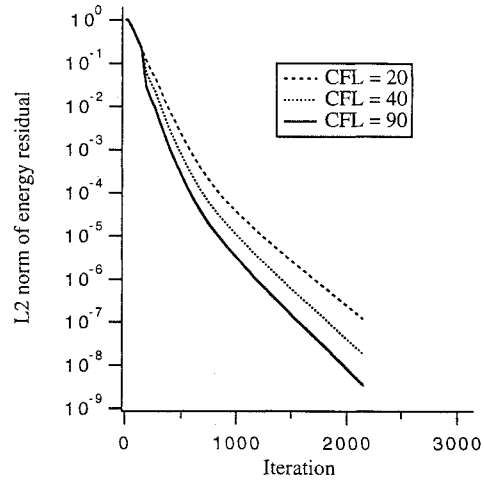

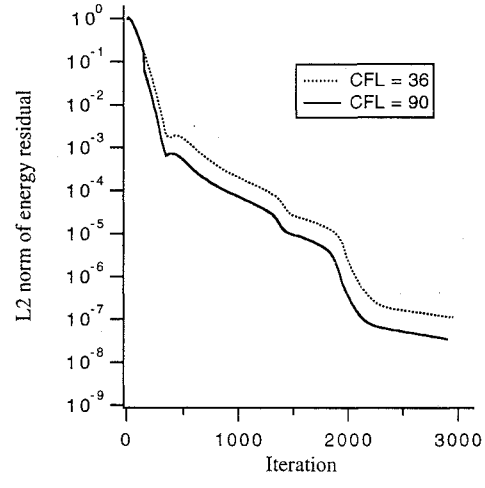

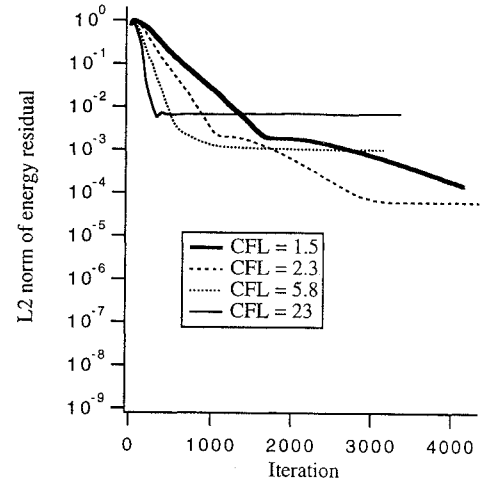

Fig. 5 Convergence histories, LUSGS method: a) Mach 15, b) Mach 30, and c) Mach 40.

of 2.3, the residual profile was similar to that produced by the point implicit method.

There are several possible reasons besides chemical stiffness why the solution algorithm performance worsened when the Mach number was increased. In the LUSGS method, the implicit flux Jacobians of the inviscid fluxes are split into positive and negative components and then differenced using one-sided differences. The viscous, which are centrally differenced, are not treated implicitly. The viscous terms might, therefore, affect the performance of the method.

A comparison was made in the behavior of the LUSGS method with and without viscous terms. The algorithm was run at Mach 30 at CFL numbers of 36 and 90. The results are shown in Fig. 6a. There is very little difference in the residual profiles with or without viscous terms, so viscous terms would not appear to be the cause of the diminished performance. They do have some effect on the stability of the method. When the viscous terms were removed, it was possible to run the code at a CFL number of 179. The results obtained without viscous terms at CFL numbers 36, 90, and 179 are shown in Fig. 6b. There is not a substantial difference in the three residual histories.

Another possible reason for the diminished performance could be grid resolution effects. The spatial resolution might be insufficient to resolve the chemical gradients. Computations were performed using an axisymmetric version of the code with a 49 × 49 grid,

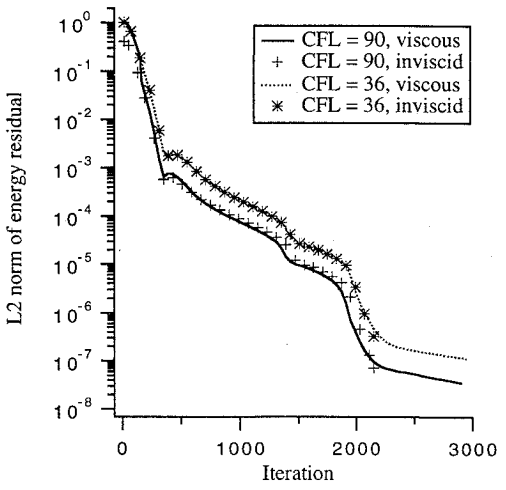

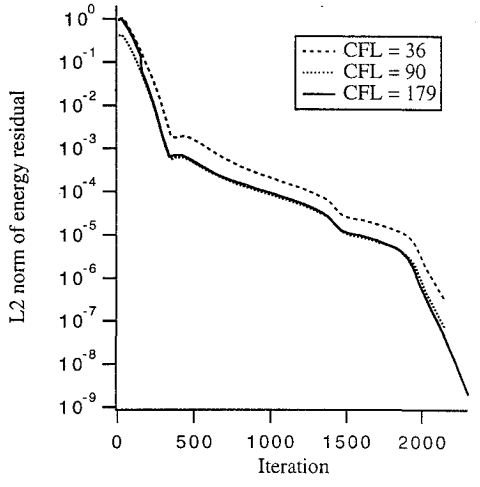

Fig. 6 Effect of viscosity, LUSGS method: a) viscous effects and b) inviscid LUSGS.

equivalent to one plane of the three-dimensional grid. The computation was repeated using an 89 × 89 grid. This represents a uniform increase in the spatial resolution throughout the computational domain. An axisymmetric computation was performed to reduce the computer time necessary, but the axisymmetric solution was found to converge in a similar fashion to a three-dimensional zero-angle-of-attack calculation. Doubling the number of grid points reduces the Damkohler number in the flowfield by reducing the characteristic time of translation in each computational cell.

Figure 7 shows the results of this test using the point implicit and LUSGS methods. Solutions using the 49 × 49 and 89 × 89 grids show similar convergence profile shapes. The 49 × 49 and 89 × 89 grid solutions for both methods show a leveling off in the rate of convergence after the residual drops three orders of magnitude. The point in the computation when the residual levels off with the 89 × 89 grid occurs after twice the number of iterations as the 49 × 49 grid. Increasing the spatial resolution by a factor of four everywhere in the computational domain does not seem to alleviate the performance dropoff of either method. The uniformly increased spatial resolution reduces the convergence rate while maintaining the same profile shape for both methods.

Another possibility is that grid dependencies in the shock region are affecting the convergence characteristics. The highest temperatures and, therefore, fastest reaction rates occur behind the bow shock. The adaptive grid code SAGE[17] was used to increase the spatial resolution in the shock region by adapting the original grid to the solution. This reduces the Damkohler number in the region of the bow shock. Results using the explicit under-relaxation and LUSGS methods with the original and adapted grids at Mach 30 are shown in Fig. 8a. There is no improvement in the performance of the explicit under-relaxation method when an adapted grid is used. The

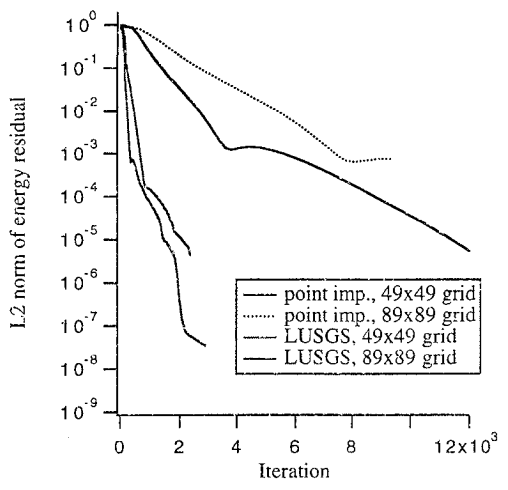

Fig. 7 Grid dependency study, Mach 30.

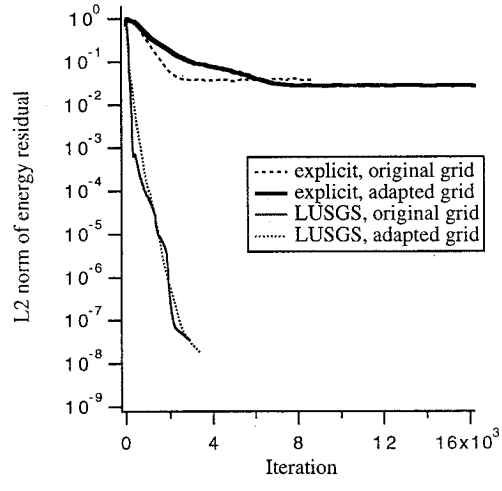

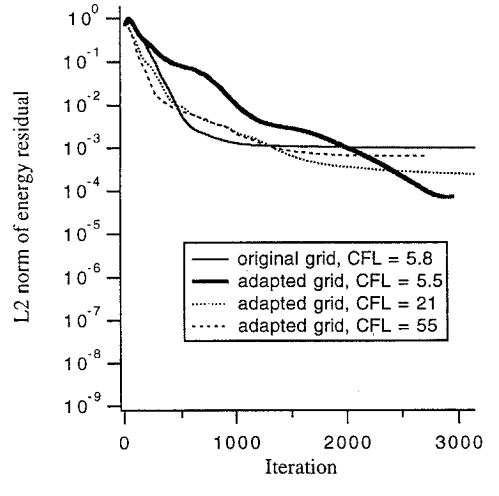

Fig. 8 Effect of grid adaption: a) grid comparison, Mach 30 and b) grid comparison, LUSGS, Mach 40.

initial convergence rate is lower, and both the original and adapted grid residual profiles asymptote to the same value. The convergence profile for the LUSGS method using the adapted grid is smoother than that obtained using the original. Both solutions obtain the same overall rate of convergence.

The effect of using the LUSGS method with an adapted grid at Mach 40 is shown in Fig. 8b. The solution does not converge using the adapted grid when the algorithm is run at a CFL number of 55 or 21. When the CFL number is reduced to 5.5, the performance of the method is improved using the adapted grid, although the overall

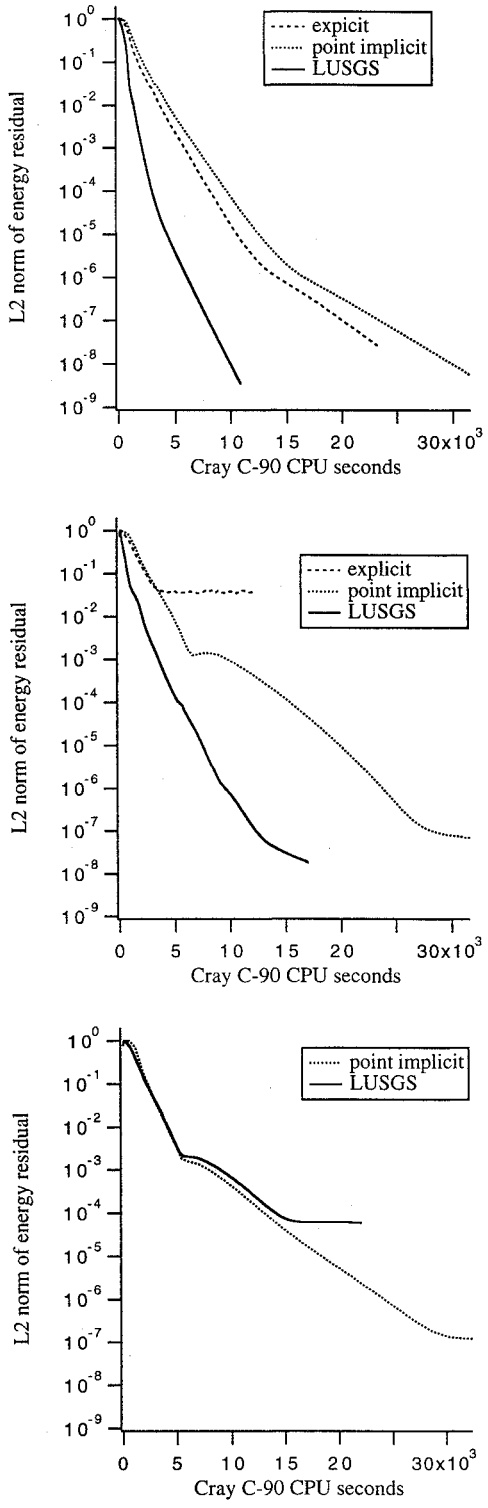

Fig. 9 Algorithm comparison in terms of computer time usage: a) Mach 15, b) Mach 30, and c) Mach 40.

convergence level achieved after 3000 steps is not significantly different from that obtained using the original grid at a CFL number of 2.3.

Figure 9 compares the solution algorithms against each other in terms of convergence vs Cray C-90 CPU time expended. The results presented here might vary from code to code depending on the level of vectorization employed. The point implicit and LUSGS algorithms both required one 10×10 matrix inversion per point per step. The matrix inverter was highly vectorized, utilizing an inner loop of length 26,411 ($49 \times 11 \times 49$). All three methods used the same evaluation of the explicit terms, the terms on the right-hand side of Eq. (5). In this study, the explicit under-relaxation method required 72.9 μs per point per step or 1.44 s per step on a $49 \times 11 \times 49$ grid. The point implicit method used 1.93 s per step, and the LUSGS algorithm required 5.07 s per step.

Results at Mach 15 are presented in Fig. 9a. The LUSGS algorithm produces an eight order of magnitude drop in the $L2$ norm of the energy residual in one-third the CPU time of the point implicit or explicit under-relaxation methods. The explicit under-relaxation algorithm outperforms the point implicit method by a smaller margin.

At Mach 30, the performance of the LUSGS method has deteriorated, but the algorithm still produces an eight order of magnitude drop in the residual in half the CPU time of the point implicit method as shown in Fig. 9b. The explicit under-relaxation method failed to produce a converged solution at this Mach number. At Mach 40, the LUSGS algorithm no longer outperforms the point implicit method. To achieve a converged solution, it was necessary to severely reduce the CFL number with the LUSGS method. From Fig. 9c, it is not apparent whether the LUSGS method would achieve the seven order of magnitude drop in residual achieved by the point implicit algorithm.

The three solution algorithms yielded essentially the same steady-state solution, as they should since all three use the same right-hand-side elements. When the explicit under-relaxation algorithm would break down, the solution would oscillate between two chemical states. At a given point the temperature might oscillate between, say, 5200 and 5220 K with a corresponding oscillation in species mass fraction and the other flow quantities.

Summary and Conclusions

Three solution algorithms are used to compute nonequilibrium flow around the Apollo 4 return capsule at 62-km altitude. By varying the Mach number, the efficiency and robustness of the solution algorithms were tested for different levels of chemical stiffness.

The point implicit method was able to converge at all Mach numbers at CFL numbers close to the explicit limit of 1.0. The shape of the residual profiles was not affected by increasing CFL number. The method showed only a slight performance degradation with increasing chemical stiffness.

The explicit under-relaxation algorithm achieved convergence only at Mach 15 and then only for a CFL number below 0.9. Above Mach 15, the method would only converge one order of magnitude before residual profile began oscillating.

The CFL number does not affect the shape of the LUSGS residual profile at Mach 30 and below. Effective convergence is possible at high CFL numbers. At Mach 40, the LUSGS method only converged if the CFL number was reduced to a low value, 2.3 in this study. Even then the residual decreases only four orders of magnitude before leveling off.

The fact that the viscous terms were evaluated explicitly did not affect the convergence rate or account for the performance dropoff of the LUSGS method at Mach 30 although it did affect the stability. When the solution algorithm is run inviscid it is possible to use a higher CFL number.

The performance trends of the three solution algorithms seem to be grid independent. When the spatial resolution was uniformly increased by doubling the number of grid points in each direction, the convergence rate of the point implicit and LUSGS algorithms slowed, but the shape of the residual profiles remained unchanged. The use of a solution-adapted grid did not improve the performance of the explicit method. The residual sill flattened out after converging one order of magnitude. For the LUSGS algorithm the residual profile was smoother using the adapted grid, but the overall convergence rate was unchanged at Mach 30. At Mach 40 the LUSGS method showed a slight performance improvement using the adapted grid, but the rate of convergence was still much lower than that seen with the LUSGS algorithm at Mach 30.

At low levels of chemical stiffness, the LUSGS algorithm outperforms both the point implicit and explicit under-relaxation methods. At Mach 15, LUSGS used one-third the Cray C90 computer time to achieve the same level of convergence. As chemical stiffness increases, all three methods show a performance dropoff. At Mach 30, the explicit under-relaxation method cannot produce a converged solution. The convergence rate of the LUSGS method

slows more rapidly than the point implicit, but at Mach 30 LUSGS can still achieve a given level of convergence in half the computer time.

As the Damkohler numbers continue to increase, the performance of the LUSGS method continues to degrade relative to point implicit. At Mach 40 there was no advantage to using LUSGS. The rate of convergence of the LUSGS algorithm was slightly less than that of point implicit, and LUSGS could not achieve the same level of convergence.

If an 11-species air model were used, the maximum temperature level would decrease. This would tend to reduce chemical stiffness in these high-temperature regions. It is unknown whether the overall chemical stiffness would be reduced without evaluating the Damkohler number of the reactions involving the additional ionized species. The generation and inversion of the implicit matrices would be significantly more expensive in terms of computer time.

Appendix: Viscous Terms

The shear stresses are defined as

$$\tau_{xx} = \frac{2}{3}\mu\left[2\frac{\partial u}{\partial x} - \frac{\partial v}{\partial y} - \frac{\partial w}{\partial z}\right] \qquad \tau_{xy} = \mu\left[\frac{\partial u}{\partial y} + \frac{\partial v}{\partial x}\right]$$

$$\tau_{yy} = \frac{2}{3}\mu\left[2\frac{\partial v}{\partial y} - \frac{\partial u}{\partial x} - \frac{\partial w}{\partial z}\right] \qquad \tau_{xz} = \mu\left[\frac{\partial u}{\partial z} + \frac{\partial w}{\partial x}\right]$$

$$\tau_{zz} = \frac{2}{3}\mu\left[2\frac{\partial w}{\partial z} - \frac{\partial v}{\partial y} - \frac{\partial u}{\partial x}\right] \qquad \tau_{yz} = \mu\left[\frac{\partial v}{\partial z} + \frac{\partial w}{\partial y}\right]$$

Expressions for the heat conduction terms are

$$q_x = \kappa\frac{\partial T}{\partial x} \qquad q_y = \kappa\frac{\partial T}{\partial y} \qquad q_z = \kappa\frac{\partial T}{\partial z}$$

References

[1]Tauber, M. E., Palmer, G. E., and Yang, L., "Earth Atmospheric Entry Studies for Manned Mars Missions," *Journal of Thermophysics and Heat Transfer*, Vol. 6, No. 2, 1992, pp. 193–199.

[2]Candler, G., and MacCormack, R., "The Computation of Hypersonic Ionized Flows in Chemical and Thermal Nonequilibrium," AIAA Paper 88-0511, Jan. 1988.

[3]Gnoffo, P. A., and McCandless, R. S., "Three-Dimensional AOTV Flowfields in Chemical Nonequilibrium," AIAA Paper 86-0230, Jan. 1986.

[4]Li, C. P., "Computational Aspects of Chemically Reacting Flows," AIAA Paper 91-1574, June 1991.

[5]Eberhardt, S., and Imlay, S., "A Diagonal Implicit Scheme for Computing Flows with Finite-Rate Chemistry," AIAA Paper 90-1577, June 1990.

[6]Palmer, G. E., "Explicit Thermochemical Nonequilibrium Algorithm Applied to Compute Three-Dimensional Aeroassist Flight Experiment Flowfields," *Journal of Spacecraft and Rockets*, Vol. 27, No. 5, 1990, pp. 545–553.

[7]Park, C., "A Review of Reaction Rates in High Temperature Air," AIAA Paper 89-1740, June 1989.

[8]Balakrishnan, A., "Correlations for Specific Heats of Air Species to 50000 K," AIAA Paper 86-1277, June 1986.

[9]Gnoffo, P. A., Gupta, R. N., and Shinn, J. L., "Conservation Equations and Physical Models for Hypersonic Air Flows in Thermal and Chemical Nonequilibrium," NASA TP 2867, Feb. 1989.

[10]Stull, D. R., and Prophet, H., *JANAF Thermochemical Tables*, 2nd ed., National Standard Reference Data System NBS37, June 1971, pp. 1533–1667.

[11]Jaffe, R. L., "The Calculation of High-Temperature Equilibrium and Nonequilibrium Specific Heat Data for N_2, O_2 and NO," AIAA Paper 87-1633, June 1987.

[12]Anderson, W. K., Thomas, J. L., and Van Leer, B., "Comparison of Finite Volume Flux Vector Splittings for the Euler Equations," *AIAA Journal*, Vol. 24, No. 9, 1986, pp. 1453–1460.

[13]Yoon, S., and Jameson, A., "Lower-Upper Symmetric-Gauss-Seidel Method for the Euler and Navier–Stokes Equations," *AIAA Journal*, Vol. 26, No. 9, 1988, pp. 1025, 1026.

[14]Palmer, G. E., "Improved Flux-Split Algorithm Applied to Hypersonic Flows in Chemical Equilibrium," *AIAA Journal*, Vol. 28, No. 7, 1990, pp. 1153, 1154; also AIAA Paper 88-2693, June 1988.

[15]Palmer, G. E., "Thermochemical Nonequilibrium Flow Computations of Flow Around the Aeroassist Flight Experiment," *Journal of Thermophysics and Heat Transfer*, Vol. 6, No. 3, 1992, pp. 405–411.

[16]Ried, R. C., Rochelle, W. C., and Milhoan, J. D., "Radiative Heating to the Apollo Command Module: Engineering Prediction and Flight Measurement," NASA TM X-58091, April 1972.

[17]Davies, C. B., and Venkatapathy, E., "The Multidimensional Self-Adaptive Grid Code, SAGE," NASA TM-103905, July 1992.